

Origami acoustics: using principles of folding structural acoustics for simple and large focusing of sound energy

This content has been downloaded from IOPscience. Please scroll down to see the full text.

2016 Smart Mater. Struct. 25 085031

(<http://iopscience.iop.org/0964-1726/25/8/085031>)

View [the table of contents for this issue](#), or go to the [journal homepage](#) for more

Download details:

IP Address: 164.107.169.192

This content was downloaded on 19/12/2016 at 21:35

Please note that [terms and conditions apply](#).

You may also be interested in:

[Ultrathin thermoacoustic nanobridge loudspeakers from ALD on polyimide](#)

J J Brown, N C Moore, O D Supekar et al.

[Material selection for elastic energy absorption in origami-inspired compliant corrugations](#)

Sean S Tolman, Isaac L Delimont, Larry L Howell et al.

[Fluidic origami: a plant inspired adaptive structure with shape morphing and stiffness tuning](#)

Suyi Li and K W Wang

[Lattice Boltzmann simulations of sound directivity of a cylindrical pipe with mean flow](#)

Yong Shi, Andrey R da Silva and Gary P Scavone

[Origami interleaved tube cellular materials](#)

Kenneth C Cheung, Tomohiro Tachi, Sam Calisch et al.

[Active control of far-field sound radiation by a beam with piezoelectric control transducers: physical system analysis](#)

Bor-Tsuen Wang

[Geometric design and mechanical behavior of a deployable cylinder with Miura origami](#)

Jianguo Cai, Xiaowei Deng, Jian Feng et al.

[Features in geometric receiver shapes modelling bat-like directivity patterns](#)

Francesco Guarato, Heather Andrews, James F C Windmill et al.

[Design of arrays for acoustic sounder antennas](#)

T J Mousley, D N Asimakopoulos, R S Cole et al.

Origami acoustics: using principles of folding structural acoustics for simple and large focusing of sound energy

Ryan L Harne and Danielle T Lynd

Department of Mechanical and Aerospace Engineering, The Ohio State University, Columbus, OH 43210, USA

E-mail: harne.3@osu.edu

Received 27 January 2016, revised 4 May 2016

Accepted for publication 20 May 2016


Published 19 July 2016



CrossMark

Abstract

Fixed in spatial distribution, arrays of planar, electromechanical acoustic transducers cannot adapt their wave energy focusing abilities unless each transducer is externally controlled, creating challenges for the implementation and portability of such beamforming systems. Recently, planar, origami-based structural tessellations are found to facilitate great versatility in system function and properties through kinematic folding. In this research we bridge the physics of acoustics and origami-based design to discover that the simple topological reconfigurations of a Miura-ori-based acoustic array yield many orders of magnitude worth of reversible change in wave energy focusing: a potential for acoustic field morphing easily obtained through deployable, tessellated architectures. Our experimental and theoretical studies directly translate the roles of folding the tessellated array to the adaptations in spectral and spatial wave propagation sensitivities for far field energy transmission. It is shown that kinematic folding rules and flat-foldable tessellated arrays collectively provide novel solutions to the long-standing challenges of conventional, electronically-steered acoustic beamformers. While our examples consider sound radiation from the foldable array in air, linear acoustic reciprocity dictates that the findings may inspire new innovations for acoustic receivers, e.g. adaptive sound absorbers and microphone arrays, as well as concepts that include water-borne waves.

 Online supplementary data available from stacks.iop.org/SMS/25/085031/mmedia

Keywords: origami, sound radiation and reception, tessellations, acoustics, Miura-ori

(Some figures may appear in colour only in the online journal)

1. Introduction

Focused acoustic energies are the fuel for numerous scientific and engineering applications including biomedical and industrial imaging [1–5], target destruction [6, 7], signal and message transmission [8, 9], and acoustic environment simulation [10–12], to name a few. An individual electro-mechanical acoustic transducer, whether serving as a microphone or loudspeaker, exhibits a spatially-varying sensitivity to the radiation or reception of acoustic waves, a characteristic that also changes based on the transducer shape and acoustic wave frequency. This property is called ‘directivity’ and it is the same for both radiated and received waves according to

the principle of linear acoustic reciprocity [13]. Although planar transducer shapes inherently exhibit a moderate directive sound-focusing capability at frequencies corresponding to wavelengths shorter than the largest transducer dimension, to significantly focus acoustic energies at any frequency it is the convention to utilize arrays of such transducers in two-dimensional grids, for instance a speaker array. In such a configuration, phase differences associated with the waves’ times-of-flight from each transducer result in large constructive interference at locations in space where it is desired to focus the acoustic energy for the application [14].

Building from this basis, the approach of assembling and controlling arrays of acoustic transducers is termed

'beamforming'. By actively introducing phase delays to the incoming or outgoing signals among each transducer within the array, the directivity of the array is selectively focused, intensified, and steered rather than remaining limited to that associated with the inherent spatial distribution of the array transducers [15]. While beamforming technology performance has advanced over the years for new generations of microphone and loudspeaker arrays, the approaches typically require non-trivial electronic signal processing and computational power thus compromising and/or complicating their simple, real-time implementation [11, 16]. In addition, the technologies often employ physically large arrays due to the need for spatially-distributed transducers to accommodate the inherent limitations of phased-array technologies which creates an adverse trade-off between desirable performance and valuable portability [17–20]. These long-standing challenges in beamforming applications—implementation (computational) complexity and system portability—suggest that alternative concepts for acoustic energy focusing, unconventional though they may be, should be openly considered if they are capable of providing viable resolutions or offer the promise for new beamforming functionality. Indeed, more recent advances in parametric acoustic arrays are exploring completely different phenomena to focus sound energy, albeit with their own trade-offs in spectral bandwidth, complexity and performance [21–25].

Another emerging field of research has leveraged arrays of planar elements for vastly different purposes. Using ordered planar tessellations, investigators have shown that origami-inspired structural/material system design may empower favorable characteristics due to folding-induced changes of the topology. Such folding of two-dimensional planar structures introduces three-dimensional functionality [26, 27] and alters fundamental properties like stiffness and Poisson's ratio when the system is used for structural purposes [28–30]. As a result, origami-inspired science and engineering developments have recently produced myriad innovations in reprogrammable mechanical and material systems [29, 31], multistable, morphing architectures [32, 33], deployable surfaces [34, 35], and simple actuators [36, 37], with advancements in such folding engineered systems spanning the meter [38] to nanometer [39] scales.

These discoveries of origami-based engineering design unequivocally indicate that *folding* structures from two-dimensional *planar tessellations* is the source of desirable system characteristics. As described above, such a two-dimensional architecture of planar elements is likewise a common basis for developing acoustic arrays, and it is well-known that the spatial distribution of transducer elements is critically tied to the sound energy-focusing capability of acoustic arrays [40, 41]. Yet, the conventional, fixed-transducer arrays lack a versatility of energy-focusing performance, which has thus led researchers to establish computational beamforming methods that enhance the underlying arrays' utilities.

Drawing an analogy between the planar surfaces of acoustic transducer arrays and the planar facets of origami tessellations, we see a prime opportunity to explore a new

concept for foldable acoustic arrays to surmount the challenges of traditional, active beamforming methods via the adaptation of acoustical sensitivities by straightforward folding procedures. In fact, this new concept offers solutions to both long-standing challenges of active beamforming approaches. First, by using folding rules to reconfigure a tessellated acoustic array and thus to adapt the system directivity and energy-focusing capabilities, only one drive or detection signal is required for the array since all planar transducers are able to be driven or sensed in parallel: a great simplification of implementation. Conveniently, the need for only one signal also eliminates the costly computational signal processing and enables real-time, on-demand control of acoustic energy focusing by mechanical reconfiguration of the tessellated array. Secondly, numerous origami tessellations are flat-foldable which means that they possess two configurations exhibiting zero volume: unfolded and fully-folded states [42]. Thus, a tessellated acoustic array that is flat-foldable represents an innovation for beamforming systems because it may be fully compacted for ease of transport and later deployed by unfolding for its utilization in acoustic energy focusing and steering.

Therefore, by bridging the physics of acoustics with the recent discoveries drawn from origami-based science, in this research we take a first look at the on-demand tunability of vibroacoustic properties realized through the straightforward folding kinematics of a tessellated acoustic array. Although our investigations exemplify the promise of this new concept to guide radiated acoustic waves in air, linear acoustic reciprocity dictates that the new principles apply equally well to the 'sensing' acoustic mode, such as for adaptive microphone arrays and sound energy absorbing materials, and may be harnessed in other fluid media supporting linear wave propagation, including water [13, 43]. For the proof-of-concept studies conducted in this research, the intent is to identify the potential of the new concept, which contrasts to an alternative strategy of comprehensively comparing the performance capabilities of this emergent idea to previously developed computational beamforming technologies. On the other hand, such characterization is part of our ongoing research pursuits and interests.

Thus, as carried out for this research, the following sections describe the tessellated array architecture considered throughout this study and details the analytical and experimental methods undertaken to explore the system. The theoretical and analytical results are then reported and discussed from which we uncover and clarify the new opportunities cultivated at the interface of origami and acoustics.

2. Analytical and experimental methods

We study the Miura-ori tessellation as the basis for an array of parallelogram-shaped acoustic pressure radiators, figure 1(a). The Miura-ori tessellation is selected for this examination based on its previous adoption for industrial and commercial purposes [34, 44] which exemplifies its practicality for fabrication and diverse, applied implementation. The repeated

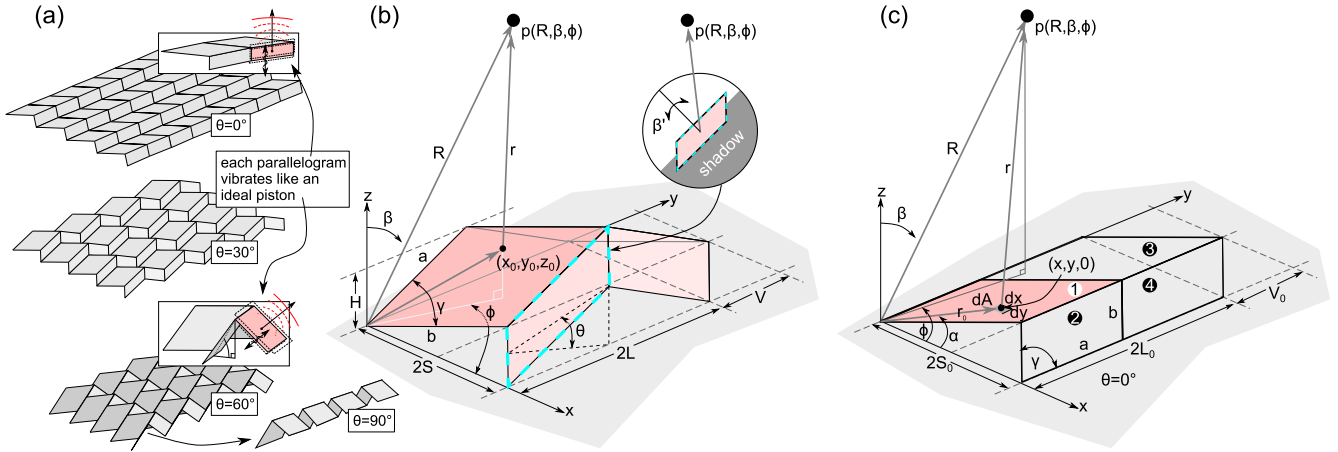


Figure 1. (a) Miura-ori folding kinematic trends and ideal-piston vibration of each parallelogram. (b) Analytical model notation to predict the pressure at the field point $p(R, \beta, \phi, t)$. The inset illustrates that folding leads to a reduction in radiating angles that contribute to the far field pressure point. (c) Analytical model notation developed upon the unfolded Miura-ori unit cell topology.

Miura-ori unit cell is shown in figure 1(b), and includes four parallelograms geometrically related through edge lengths a and b , edge angle γ , and folding angle θ .

2.1. Rayleigh's integral formulation to analyze acoustic wave radiation from a folding, tessellated array

A lossless, structural-acoustic model is formulated to gain essential insights by predicting the acoustic pressure at far field point $p(R, \beta, \phi, t)$ —a distance R , elevation angle β , and azimuthal angle ϕ away from the origin—due to the single-frequency, normal surface acceleration of each parallelogram assembled into an array of the Miura-ori cells numbering M_x by M_y in the x and y axes, respectively, illustrated in figure 1(a). In other words, each parallelogram facet is assumed to vibrate like an ideal, rigid, baffled piston such that pressure waves are radiated into the acoustic fluid above the plane $(x, y, 0)$. Because of the folding-induced rotation and translation of the parallelogram-shaped and piston-like radiators, the phase differences of pressure waves arriving at the field point from each facet superimpose uniquely based on the folding angle θ and field point location (R, β, ϕ) . Thus, as provided by this new model formulation, a direct link is created between the kinematically-defined formation of the tessellated array and the acoustic spectral and spatial sensitivities for pressure radiation to the field point. In fact, this technical approach may be compared to certain shape-changing, adaptive radio frequency (RF) antennae [45, 46] including recent advancements to create frequency selective surfaces by folding RF antennae in patterns inspired by origami tessellations [47].

When the mechanical impedance of a baffled, vibrating structural surface is much greater than the acoustic impedance (such as for a stiff structural panel interfaced with air, hereafter assumed), the relation between the spatially distributed harmonic oscillations of the surface and the resulting pressure change at a point in space away from the surface is examined

by evaluating Rayleigh's integral [43]:

$$p(R, \beta, \phi, t) = j \frac{\rho_0 \omega u_0}{2\pi} e^{j\omega t} \int_A \frac{e^{-jkr}}{r} dA. \quad (1)$$

Figure 1(b) details the structural acoustic unit cell for a folded configuration $\theta > 0$ while figure 1(c) presents the unfolded topology and corresponding notations. From equation (1), one has that $\rho_0 = 1.104 \text{ kg m}^{-3}$ is the air density; ω is the angular frequency of oscillation of the surface; u_0 is the spatially-uniform, normal, velocity amplitude of the structure-fluid interfacing surface; A is the surface area of the array; $k = \omega/c$ is the acoustic wavenumber, with $c = 340 \text{ m s}^{-1}$ as the sound speed; while r is the distance from an oscillating differential area element dA to the far field pressure point $p(R, \beta, \phi, t)$ that is a distance R from the reference origin and angularly positioned according to angles β in elevation and ϕ in azimuth. The Miura-ori cell is repeated in the $x-y$ plane by M_x and M_y times, respectively, to construct the tessellated array, figure 1(a). Focusing first on the unfolded topology, figure 1(c), it is assumed that each parallelogram-shaped, piston-like facet contributes to the total integration of equation (1) while the array is itself enclosed in a rigid baffle where the normal velocity is zero. It is also assumed that the array remains attached to the $x-y$ plane and does not exhibit modal oscillations associated with the whole structural dimensions. These three assumptions are easily met in the experiments as described in the following section.

Geometrically, the distance r is related to the reference distance R according to

$$r = [R^2 + r_0^2 - 2Rr_0 \sin \beta \cos(\phi - \alpha)]^{1/2}. \quad (2)$$

This expression can be reduced assuming that the location of the pressure point is in the far field. Subject to far field approximation [48], the r becomes $r \approx R$ in the denominator of equation (1), while the complex exponential (oscillatory) argument must retain the fundamental phase information

according to

$$r \approx R - r \sin \beta \cos(\phi - \alpha). \quad (3)$$

Substituting these results along with geometric relations $-x = r \cos \alpha$, $y = r \sin \alpha$, and $dA = dx dy$ —into equation (1), one obtains for the unit cell

$$p_{\text{cell}}(R, \beta, \phi, t) = j \frac{\rho_0 \omega u_0}{2\pi} e^{j\omega t} \frac{e^{-jkR}}{R} \times \int_A e^{j(\Psi_1 x + \Psi_2 y)} dx dy \quad (4)$$

given that $\Psi_1 = k \sin \beta \cos \phi$ and $\Psi_2 = k \sin \beta \sin \phi$.

Due to the folding of the Miura-ori array, the unfolded spatial extents S_0 , L_0 , and V_0 , figure 1(c), are modified to [28]:

$$S = b \frac{\cos \theta \tan \gamma}{\sqrt{1 + \cos^2 \theta \tan^2 \gamma}}, \quad (5)$$

$$L = a \sqrt{1 - \sin^2 \theta \sin^2 \gamma}, \quad (6)$$

$$V = b \frac{1}{\sqrt{1 + \cos^2 \theta \tan^2 \gamma}}, \quad (7)$$

$$H = a \sin \theta \sin \gamma, \quad (8)$$

where H is the height of the Miura cell induced by fold angles $\theta > 0$, figure 1(b). During folding, the geometric center of each parallelogram facet increases in height from the reference plane by the same amount $H/2$. This quantity is negligible in comparison to R when employing far field approximations, and thus is safely neglected from the following computations of the Rayleigh's integral since it contributes to a minor change in the term that influences all angular coordinates uniformly according to $\frac{e^{-jkR}}{R} \rightarrow \frac{e^{-jk(R-H/2)}}{R-H/2}$. On the other hand, the folding causes each facet to translate and rotate with respect to the reference (x, y, z) system. These motions modify the appropriate area integration limits for each facet in equation (4) and alter the far field elevation angle β region over which a given facet contributes a directly radiated pressure wave to the far field point. To account for these influences of folding, equation (4) is written for the unit cell as

$$p_{\text{cell}}(R, \beta, \phi, t) = j \frac{\rho_0 \omega u_0}{2\pi} e^{j\omega t} \frac{e^{-jkR}}{R} \sum_{i=1}^4 v_i, \quad (9)$$

$$v_1 = \int_0^{S_0} \int_{y_1(x)}^{y_2(x)} e^{j\Psi_{11}y} dy \cdot e^{j\Psi_{12}x} dx \text{ for parallelogram 1,} \quad (10)$$

$$v_2 = \int_S^{S+S_0} \int_{y_3(x)}^{y_4(x)} e^{j\Psi_{21}y} dy \cdot e^{j\Psi_{22}x} dx \text{ for parallelogram 2,} \quad (11)$$

$$v_3 = \int_0^{S_0} \int_{y_5(x)}^{y_6(x)} e^{j\Psi_{31}y} dy \cdot e^{j\Psi_{32}x} dx \text{ for parallelogram 3,} \quad (12)$$

$$v_4 = \int_S^{S+S_0} \int_{y_7(x)}^{y_8(x)} e^{j\Psi_{41}y} dy \cdot e^{j\Psi_{42}x} dx \text{ for parallelogram 4,} \quad (13)$$

where, for the Miura-ori cell in the i th row of an array with M_y rows, the integration limits are

$$y_1(x) = \frac{V_0}{S_0}x; y_2(x) = L_0 + \frac{V_0}{S_0}x, \quad (14)$$

$$y_3(x) = -\frac{V_0}{S_0}x + V_0 + \frac{V_0}{S_0}S; y_4(x) = -\frac{V_0}{S_0}x + L_0 + V_0 + \frac{V_0}{S_0}S, \quad (15)$$

$$y_5(x) = \frac{V_0}{S_0}x + L; y_6(x) = L + L_0 + \frac{V_0}{S_0}x, \quad (16)$$

$$y_7(x) = -\frac{V_0}{S_0}x + L + V_0 + \frac{V_0}{S_0}S; y_8(x) = -\frac{V_0}{S_0}x + L + L_0 + V_0 + \frac{V_0}{S_0}S. \quad (17)$$

The complex exponential arguments utilize the expressions

$$\Psi_{11} = k \sin(\beta + \theta) \cos \phi_1; \Psi_{12} = k \sin(\beta + \theta) \sin \phi_1 \quad (18)$$

$$\Psi_{21} = k \sin(\beta + \theta) \cos \phi_2; \Psi_{22} = k \sin(\beta + \theta) \sin \phi_2 \quad (19)$$

$$\Psi_{31} = k \sin(\beta - \theta) \cos \phi_1; \Psi_{32} = k \sin(\beta - \theta) \sin \phi_1 \quad (20)$$

$$\Psi_{41} = k \sin(\beta - \theta) \cos \phi_2; \Psi_{42} = k \sin(\beta - \theta) \sin \phi_2 \quad (21)$$

having defined

$$\phi_1 = \phi + \alpha - \alpha^*,$$

$$\phi_2 = \phi - \alpha - \alpha^*,$$

$$\alpha^* = (\pi/2) - \gamma,$$

$$\alpha(\theta) = \cos^{-1} [\cos \theta \tan \gamma (1 + \cos^2 \theta \tan^2 \gamma)^{-1/2}].$$

The computation of the Rayleigh's integral equation (9) is subject to the following constraints

$$\text{if } \beta + \theta < \pi/2 \text{ and } \beta - \theta > -\pi/2, \text{ then } p_{\text{cell}}(R, \beta, \phi, t) = j \frac{\rho_0 \omega u_0}{2\pi} e^{j\omega t} \frac{e^{-jkR}}{R} \sum_{i=1}^4 v_i. \quad (22)$$

For elevation and folding angle combinations outside of the range indicated in equation (22), one of the facet types, numbered 1–4 in figure 1(c), exhibits an acoustic shadow with respect to the point in the far field, as illustrated in the inset of figure 1(b). As a result, predictions may be compromised by the fact that other acoustic phenomena like reflection and diffraction would non-trivially contribute to the radiated acoustic pressure at the field point, although only the direct, line-of-sight radiation is accounted for in Rayleigh's

integral. Thus, model results determined for angular locations that fall outside of the constraints of equation (22) are omitted. We may also anticipate that model predictions approaching these limits exhibit progressively poorer accuracy with respect to the more nuanced acoustic wave front that truly reaches the field point.

Equation (22) therefore predicts the sound pressure directional sensitivities of the Miura-ori acoustic transducer unit cell. Array design principles are employed to account for the assembly of the cells into an array that spans the $x - y$ plane. Namely, the directivity of arrays of directional transducers may be determined by the product of the transducer unit cell directivity function and the array directivity function [14]. Here, the unit cell directivity is given in equation (22) by the summation. To account for M_x number of these columns and M_y number of these rows in the two-dimensional planar array, the array directivity function is [49]:

$$D(\beta, \phi) = \frac{\sin [M_x k S \sin \beta \cos \phi]}{M_x \sin [k S \sin \beta \cos \phi]} \times \frac{\sin [M_y k L \sin \beta \sin \phi]}{M_y \sin [k L \sin \beta \sin \phi]}. \quad (23)$$

The product of this directivity, equation (23), with the directivity determined from the summation in equation (22) yields the total Miura-ori acoustic array directivity function. Multiplying the total directivity by the leading terms gives the harmonic pressure change (above and below static pressure) at the field point

$$p(R, \beta, \phi, t) = j \frac{\rho_0 \omega u_0}{2\pi} M_x M_y e^{j\omega t} \frac{e^{-jkR}}{R} D(\beta, \phi) \times \sum_{i=1}^4 v_i. \quad (24)$$

Hereafter, the pressure equation (24) is normalized with respect to the total number of transducer facets given by the product $4M_x M_y$, so that arrays of different numbers of facets and cells can be more effectively compared.

A conventional metric is the sound pressure level (SPL), computed from the pressure change $p(R, \beta, \phi, t)$, equation (24), with respect to a reference pressure, here $p_{\text{ref}} = 20 \mu\text{Pa}$. The SPL is employed here to quantify the means by which topological reconfiguration of the tessellated array results in transmission of the acoustic energy to the field point at the angular coordinates (β, ϕ) . By the usage here, the SPL is evaluated in decibels, according to convention

$$\text{SPL} = 20 \log_{10} \left[\frac{p_{\text{rms}}(R, \beta, \phi, t)}{p_{\text{ref}}} \right], \quad (25)$$

where the subscript rms indicates the root-mean-square value.

The far field pressure spans azimuthal angles $\phi \in [0, \pi]$ rad and elevation angles $\beta \in (-\pi/2, \pi/2)$ rad where $\beta = 0$ is termed ‘broadside’ radiation [43]. In the following studies, we use the results of equation (25) to characterize the potential for this new concept of integrating origami-based engineering design and structural acoustics to

cultivate large and simple acoustic energy-focusing capabilities via the folding of a Miura-ori tessellated transducer array.

2.2. Experimental specimen fabrication and measurement methods

Several steps are undertaken to fabricate the experimental specimens whose measurements are reported here. Additional experimental details are given in the supplementary information. Specimens are created using polypropylene sheet (McMaster-Carr 1451T21) of thickness 0.762 mm for the underlying structural surface of the array. The shape of a Miura-ori pattern is cut and scored on the sheet using a laser cutter (Full Spectrum Laser H-20x12). The edge lengths and edge angle of the specimens are, respectively, $a = 33$ mm, $b = 30$ mm, and $\gamma = 50^\circ$. Once scored, the Miura-ori pattern on the sheet is appropriately folded.

Piezoelectric PVDF, of 28 μm thickness, with sputtered Cu–Ni electrodes (Measurement Specialties, 1-1003702-7) is cut into Miura-ori unit cell shapes with edge lengths a and b scaled to approximately 80% of the size used to prepare the polypropylene sheet. The size reductions are intended to prevent shorting between adjacent cells of PVDF. The laser cutter is used for cutting the PVDF. Copper tape with electrically conductive adhesive is bonded to adjacent PVDF cells and one final lead is used for connection to the amplified excitation; all upper electrodes are connected together and likewise for all lower electrodes. Thin, double-sided tape is used to bond the PVDF shapes to the polypropylene sheet at a time when it is folded to approximately an angle $\theta = 30^\circ$, which readily enables unfolding $\theta = 0^\circ$ and permits greater folding to approximately $\theta = 60^\circ$ at which extent the adherence of the PVDF to the folded cell is moderately reduced due to stretching. Two external leads are used to connect all upper or lower electrodes of the tessellated array; these two leads are then connected to the amplified excitation signal. The specimen whose measurements are reported here is shown in figure 2(a).

In figure 2(a), it is seen that a perimeter of non-activated facets surrounds the part of the tessellated array that is covered and activated by the PVDF. This approach is found to better baffle the array at the boundary between active and non-active facets, because the folded edges are immediately connected to other non-active surfaces (those with zero normal velocity). Practically, such an approach satisfies the baffle-related assumptions inherent in the model formulation. Beyond the effective baffle created by the non-active perimeter of facets, a more traditional baffle of medium density fiberboard (MDF) holds the transducer array in the plane during experimentation (supplementary figure 1). To entirely prevent curvature of the specimen due to the constraints imposed by the MDF baffle, small pins secure the bottom-most nodes of the tessellated array to a hard plane upon which the array rests. This setup is then positioned on a bed of acoustic foam housed in a chamber which is anechoic for frequencies greater than approximately 1.5 kHz. The array specimen is positioned at the center of a hemispherical track

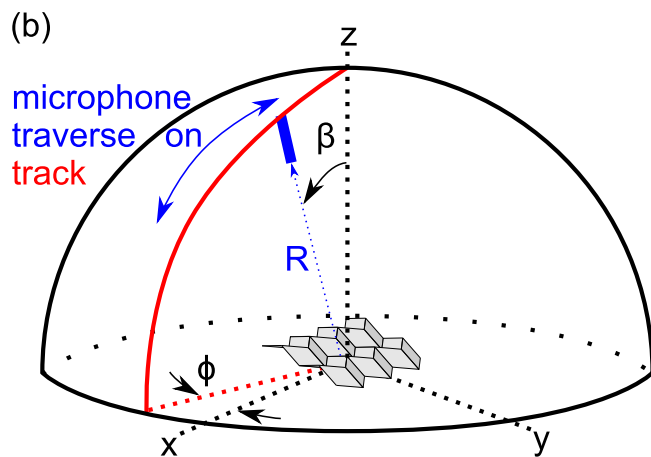
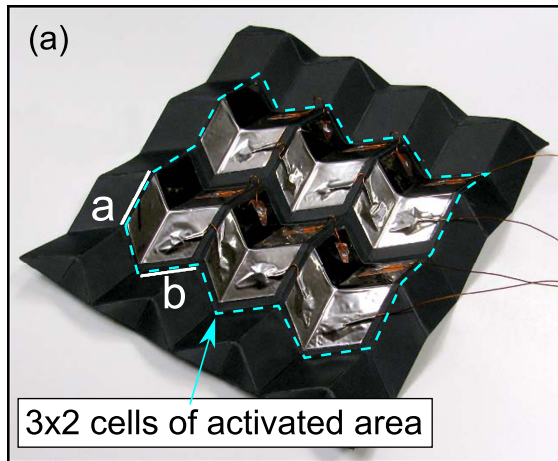


Figure 2. (a) Experimental specimen: a 3×2 cell area is covered in piezoelectric PVDF that serves to excite the facets that are covered. (b) Experimental setup to measure acoustic directivity in semi-anechoic environment, where a microphone traverses a hemispherical track according to elevation angle $\beta \in [0, 5\pi/12]$ rad with $\phi = 0$.

of radius 717.55 mm. This radial distance to the specimen plane is sufficiently well into the acoustic far field according to the standard requirements for the frequencies measured here [48]. The track is used as a guide for a traversing microphone (PCB Piezotronics 130E20) to move along elevation angle $\beta \in [0, 5\pi/12]$ rad with $\phi = 0^\circ$ that measures the far field acoustic pressure radiated from the transducer at the center, figure 2(b). For the experiments, a function generator (Siglent SDG1025) creates a single frequency wave sent to an amplifier (AudioSource AMP100) and then through an audio output transformer (RadioShack 2731380) to increase the voltage delivered to the piezoelectric PVDF that drives the transducer array. A National Instruments data acquisition system (NI 9220) obtains the pressure measurements which are evaluated through the MATLAB Data Acquisition Toolbox for processing. Data is digitally filtered using a fourth-order Butterworth filter from 1 to 18 kHz prior to evaluating the far field SPL.

3. Analytical and experimental results and findings

Bringing together our theoretical and experimental efforts, in this section we report on the predicted and measured results of SPL adaptation empowered by topological reconfigurations of the Miura-ori tessellated acoustic array.

3.1. Acoustic directivity in the far field

A comparison of the far field (SPL, dB ref. $20 \mu\text{Pa}$) predicted from our analytical model and that measured experimentally for two folding angles and three frequencies is presented in figure 3. The top row shows the experimental data across all elevation angles β measured while the bottom row presents analytical results for elevation angles that do not induce acoustic shadows. The model predictions in the bottom row are truncated within the elevation angles around broadside ($\beta = 0$) that meet criteria according to equation (22). The measurements in the top row are shown with lighter shading if such elevation locations are not valid with respect to the model and thus do not permit comparison.

At the low 3 kHz frequency, figure 3 column (a), the SPL is seen to gradually reduce as elevation angle β increases for the slightly folded topology $\theta = 9^\circ$. The increased folding angle $\theta = 32^\circ$ leads to greater directional uniformity in energy propagation. These trends are observed experimentally (top row figure 3(a)) as well as predicted by the model (bottom row), and are consistent with low frequency trends for (non-foldable) acoustic arrays in general [43]. The experimental measurements at 3 kHz exhibit minor deviations in the smoothness of SPL change according to variation in elevation angle. This may be explained by the fact that only 6.33 acoustic wavelengths separate the specimen from the microphone measurement point; thus, although this is technically a far field location [48], it is possible that near field effects may distort the measurements at this low frequency to cause the less smooth change in SPL according to change in elevation angle.

At 5 kHz, figure 3 column (b), a pressure node of significant SPL decrease appears around elevation angle $\beta = \pi/4$ rad (analytical) and $\beta = \pi/3$ rad (experimental) that rotates in angular location as folding increases. Thus, an observer in the far field remains in a zone of relative silence by rotating along β respecting the reference $x - y$ plane while the tessellated array is folded from $\theta = 9^\circ$ to 32° . Due to the inherent losses in air and imperfections in fabrication, we experimentally measure that this pressure node at 5 kHz is approximately 20 dB less in amplitude than the broadside ($\beta = 0$) SPL, which is a two order-of-magnitude difference in sound power. In other words, folding the array when driven at 5 kHz introduces a powerful sound-focusing functionality by modulating the breadth of the major lobe that is centered around broadside. At 9 kHz with the array folded to $\theta = 9^\circ$, solid curves in figure 3 column (c), two pressure nodes appear experimentally and analytically, effecting about 20 dB depth each (100 times power difference) in our measurements. Upon folding from $\theta = 9^\circ$ to 32° , dashed curves in figure 3 column (c), one node of pressure remains but at a different

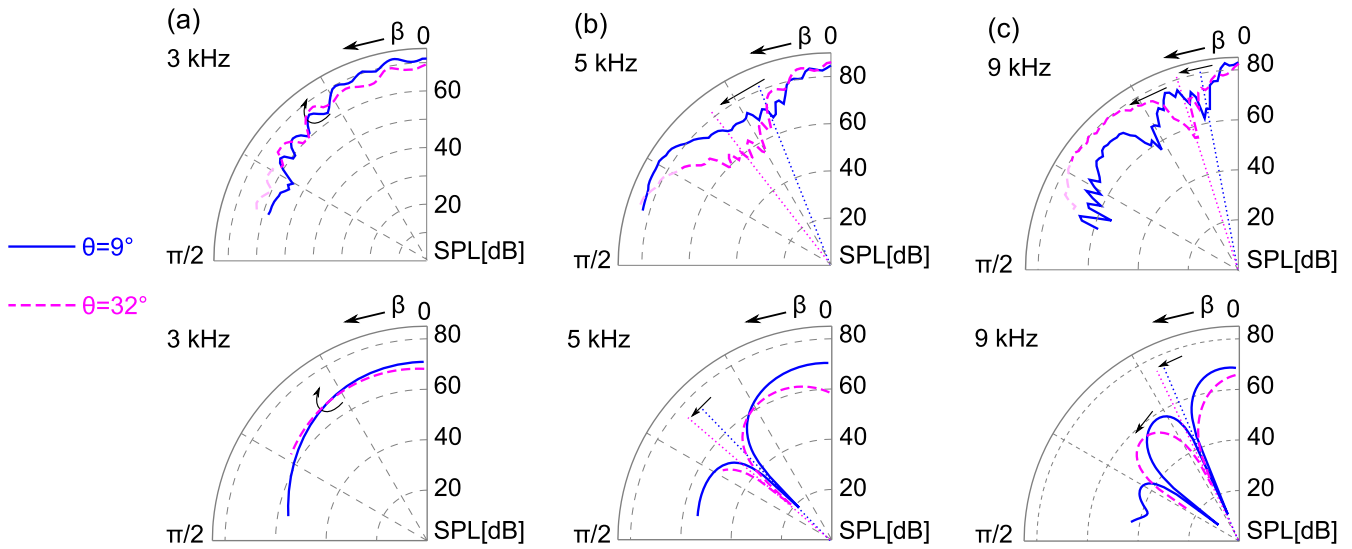


Figure 3. Sound pressure level of the array having 3×2 cells of tessellations as a function of the far field observation point elevation angle β . Measurements (top row) and analytical model predictions (bottom row). Single frequency transducer excitation at (a) 3 kHz, (b) 5 kHz, and (c) 9 kHz.

orientation in elevation β , likewise exemplifying a novel, folding-induced means to tune the concentration of energy focused within the major lobe.

3.2. Broadside spectral sensitivities induced by folding and tessellation design

The adaptive acoustic performance observed in figure 3 according to the array actuation frequency encourages an exploration of how the energy is variably focused across a wide bandwidth of frequencies at broadside, which is a common location at which acoustic waves are sought to be directed since it helps to characterize fundamental array capabilities [11]. Figure 4 presents exemplary model results for the influences of driving frequency and the edge angle γ on broadside SPL for the 3×2 cell array. For clearer understanding of the influence of the edge angles γ upon the system design, three 3×2 tessellated array configurations are shown in figure 4(b) each having a different edge angle.

For the mostly unfolded array configurations $\theta = 9^\circ$, figure 4(a), an insignificant adaptation in SPL is effected for a given excitation frequency by adjustment of the edge angle γ design variable. At higher frequencies and greater fold angles, figures 4(b) and (c), a substantially greater change in the normalized SPL may occur by tailoring the array edge angle. The white data points exemplify such change. At fold angle $\theta = 32^\circ$ and edge angle $\gamma = 29.7^\circ$, figure 4(b), the acoustic energy around 3.3 kHz is over 25 dB greater than that at 5.1 kHz (>300 times difference in power). In contrast, figure 4(c) shows that the same frequency and edge angle comparisons for an array folded to $\theta = 60^\circ$ reverses the energy focusing trend: now, the sound focused at broadside at 5.1 kHz is 20 dB greater than that achieved at 3.3 kHz. In other words, the spectral sensitivities feature significant and

tunable acoustic power focusing at broadside according to the reversible array folding and facet design.

3.3. Acoustic beamfolding for energy focusing on-demand

The results of figures 4(b) and (c) suggest that dynamic folding can facilitate significant, on-demand shaping of single-frequency sound power received by an observer in the far field at broadside. Thus, in contrast to active control of each individual transducer in a conventional two-dimensional array (i.e. beamforming), the straightforward folding of the tessellated architecture can give rise to large sound focusing at a location in space (i.e. beamfolding). In this way, the kinematic reconfiguration of the Miura-ori-based array, governed by the relations equations (5)–(8), results in a pre-determined degree of energy focusing, thus directly and simply relating the tessellated array configuration and design to acoustic performance characteristics.

As determined by the model and presented in figure 5, we characterize the influence of fold angle θ upon the far field SPL of a Miura-ori-based array spanning 3×2 and 10×9 cells' worth of the tessellation. Unshaded areas in figure 5 indicate that acoustic shadows may occur and the model composition is not suitable for prediction under such circumstances. For the 3×2 array at 5 kHz, figure 5(a), folding the array from about 10° to 40° can modulate the SPL by approximately 30 dB while further folding to 60° can raise up the SPL once again by 20 dB from the local minima near 40° . Similar influences are observed for the 10×9 array, figure 5(c), but the greater number of array elements dramatically intensifies the energy concentration to the major lobe centered on broadside. While several sidelobes of reduced amplitude appear, they are separated from the major lobe by deep pressure nodes that yield effective silence in the far field. Figures 5(b) and (d) show that similar trends occur for the

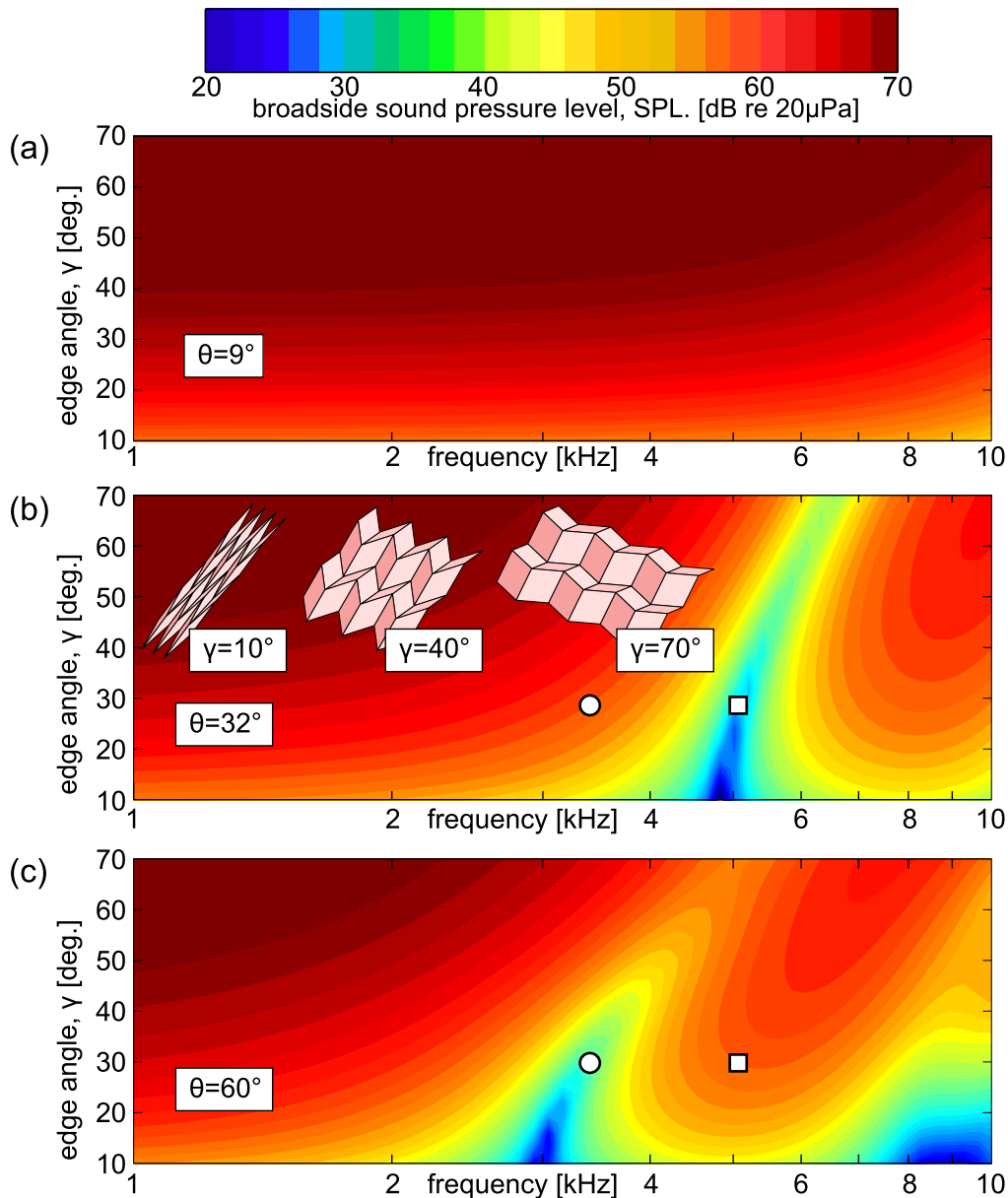


Figure 4. Broadside SPL of the array having 3×2 cells of tessellations as a function of the excitation frequency and edge angle γ . Analytical model results predicted for fold angle θ of (a) 9° , (b) 32° and (c) 60° . The array configurations shown in the top of (b) all exhibit $\theta = 32^\circ$. The circle and square points marked in (b) are respectively located at the same frequency and angle γ coordinates in (c).

3×2 and 10×9 -sized arrays, respectively, at 9 kHz, although now a local maxima of SPL occurs around a fold angle of 40° and the major lobes are considerably narrower than at 5 kHz, providing a more intense focusing of 9 kHz acoustic waves at broadside. Resulting from the topological reconfiguration, it is apparent that folding a tessellated acoustic array introduces a simple means to substantially tailor and morph the acoustic energy received in the far field. For example, at 9 kHz and with a 3×2 Miura-ori tessellated arrays, figure 5(b), dynamic folding from about 15° to 47° can promote about a 26 dB change in the SPL, which is over a 300 times difference in acoustic power. Indeed, our experimental demonstrations of the dramatic acoustic amplitude modulation driven by folding (figure 6, supplementary figure 3, and listen to supplementary audio files 1–4) exemplify the

potency of this new bridge between acoustics and origami-based science and design.

4. Discussions and conclusions

As determined from our investigations, the scale-free geometric principles of the Miura-ori tessellation [28] and scale-free acoustic principles for planar arrays operating according to the linear wave equation [43] may be synergistically combined to yield large adaptation of acoustic energy-focusing capabilities able to be leveraged in numerous applications. From the perspective of implementation, the fabrication of tessellated arrays is straightforward and may, admittedly, be improved from our experimental realization.

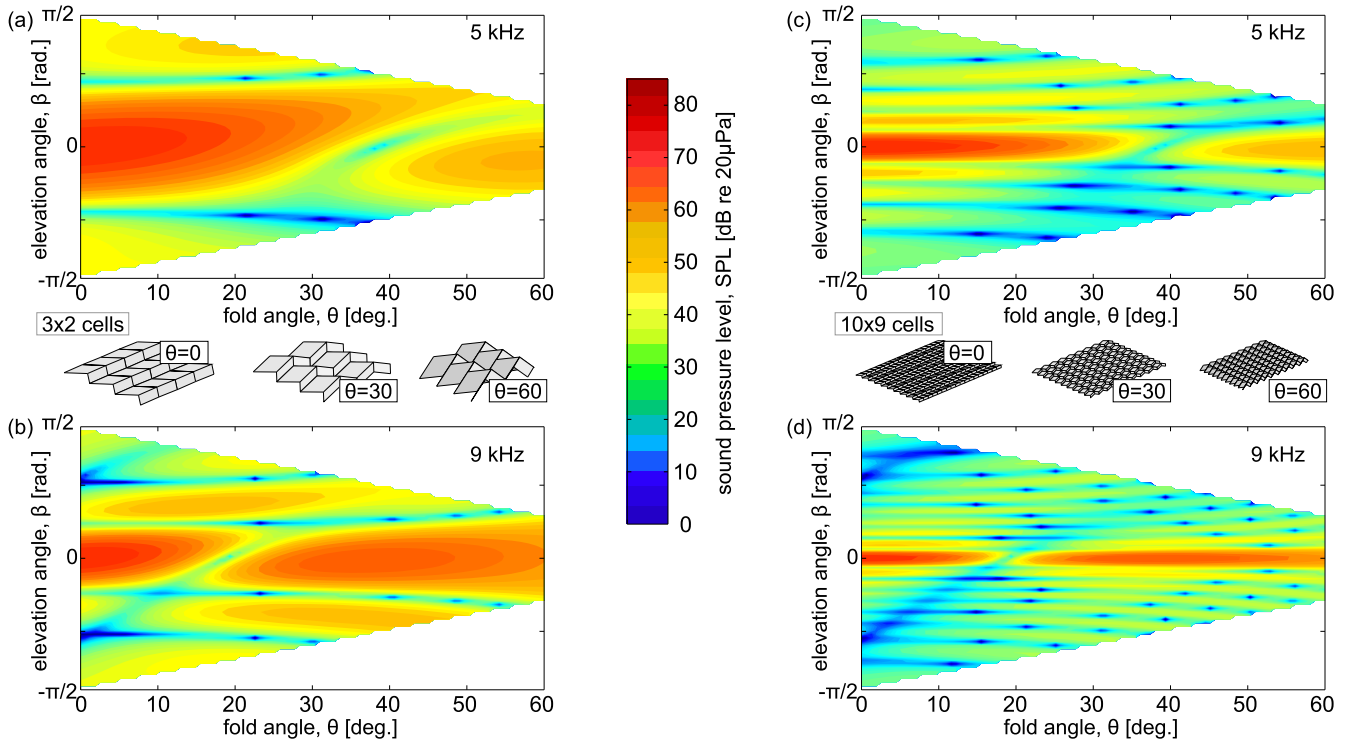


Figure 5. Far field SPL of the tessellated acoustic transducer having 3×2 (left column) or 10×9 (right column) cells as a function of elevation angle β and fold angle θ . Analytical predictions of SPL at (a) and (c) 5 kHz and (b) and (d) 9 kHz.

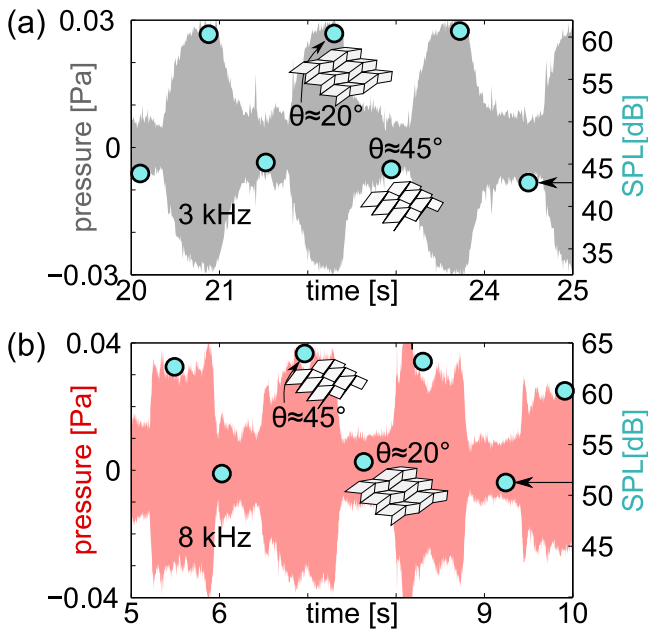


Figure 6. Sound shaping by topological reconfiguration. Experimentally recorded far field sound pressure for the tessellated array of 3×2 cells. While driven with a constant amplitude (a) 3 kHz or (b) 8 kHz frequency, the transducer is folded back-and-forth as illustrated. The circle data points (and right vertical axis) indicate the SPL of the frequency during the span of time the maintains one of the two extreme folding angles here considered. Data here correspond to portions of audio files (see supplementary information).

For instance, utilizing active laminated materials [50], including soft materials that contain internal active layers for transduction [51], may result in a more integrated design solution. However, effective transduction requires that the parallelogram surfaces remain rigid. Thus, future tessellated array concepts must provide large change of impedance between compliant, folding edges and the stiff planar surfaces that oscillate to transmit or receive acoustic energies.

The new ideas explored in this report seek to demonstrate alternative means by which the long-standing challenges of acoustic beamforming technologies may be overcome. These challenges include the complexity and computational cost of implementing an array of individually-driven or -sensed acoustic transducers for the purpose of steering sound sensitivities [12, 16, 52], and the compromised portability of such a setup due to the fixed spatial distribution of the transducers into pre-determined arrangements that facilitate the computational signal processing [15, 53]. From the results described here, the new concept of foldable tessellated acoustic arrays indeed provides resolutions to these challenges through a greatly simplified electrical implementation and complexity reduction, and through a means for substantial device compacting and portability via folding. Although it is difficult to draw a broadly meaningful comparison between this new, unconventional approach and the drastically different established beamforming technologies, acoustic beamforming using tessellated array architectures may introduce the functionality of acoustic energy focusing to applications where constraints

on complexity, size, and portability are such that traditional arrays and beamforming are unsuitable. For example, the interests in origami-based engineering systems on small scales [39]—where three-dimensional fabrication is infeasible but two-dimensional fabrication followed by three-dimensional folding/assembly are already demonstrated [26, 27, 31]—suggest that applications of acoustic energy focusing at ultrasonic frequencies for biomedical or structural/mechanical system monitoring, imaging, and manipulation are suitable outlets for the proposed beamforming technology. In addition, the deploy-ability of tessellated acoustic arrays is unparalleled with respect to most conventional beamformer arrays, particularly if one considers the electronic signal processing required to put conventional beamformers to practice [16]. Thus, applications where the delivery of an array is challenged by space or weight constraints (e.g., for long-distance air/underwater transport, or embedded applications) are likewise well-suited to implement foldable acoustic arrays that usefully deploy for their purpose once at the working site [35, 40]. While our current realizations of origami-based tessellated acoustic arrays could not replace the established beamforming technologies, the opportunities to overcome the long-standing challenges due to an unconventional approach as demonstrated first in this research suggests a promising potential worth pursuing in greater detail.

Yet, just as for any new research venture, to capitalize on the opportunity, an effective design tool is required. The analytical model formulation established in section 2.1 is a step in such a direction since it directly translates the geometric design and folded configuration of the Miura-ori tessellated acoustic array to the far field sound pressure received in consequence to the vibration of the numerous array transducers. On the other hand, discrepancies are observed in the comparison between measured and predicted results, figure 3. Considering the analytical model formulation itself, it is important to recall the assumptions inherent in the model with respect to the practical aspects involved in fabricating, configuring, and measuring the radiated sound pressure from the experimental specimens. In particular, far field and perfectly-periodic array assumptions are adopted to arrive at the closed form evaluation of the Rayleigh's integral, equation (22). Of course, as indicated above, near field influences (i.e., insufficiently developed plane waves) may distort the measurements and each facet/transducer of our current generation experimental specimen inevitably varies slightly from one to the next considering the bonding of the PVDF film to the polypropylene substrate. Such small deviations in our current manufacturing processes are a source to the discrepancies between model predictions and measured data. This is because sound energy-focusing via distributed transducers is reliant on phase differences among the propagated waves so that the desired constructive or destructive interference occurs at select points in space. The experimental proof-of-concept array considered in this research is the result of several generations' worth of specimens and designs but is still by no means perfect. A better integrated electromechanical design, such as the laminated

design described above, may result in a more consistent delivery of acoustic waves to far field points to yield the substantially greater cancellation or amplification of acoustic waves that are predicted by the analytical model. Greater precision in our manufacture of the specimens is a particular feature of our ongoing work. Advancing the modeling to a next stage, we are developing boundary element model formulations which are well-suited to the radiated sound field problems of interest here [54, 55]. In this way, our ongoing efforts seek to obtain greater quantitative agreement between measurements and predictions to facilitate the design tool required to best see these new ideas to practice.

Although the studies in this report focused on the radiation of acoustic waves in air from the tessellated array architectures, further advancements can be derived from the new concepts introduced in this research. Acoustic reciprocity—the principle that source and receiver positions can be interchanged without effecting the signal received [43]—suggests that our findings are equally applicable for any type of transmitted or received wave-borne energy governed by the linear acoustic wave equation. This indicates that sound absorbers or microphone arrays will exhibit equally intense adaptation of acoustic energy reception by leveraging the folding of tessellated architectures, while the ideas established here also apply to systems intended for water-borne waves. Surveying the outcomes, through an elegant integration of origami geometry and acoustics, this research establishes a new domain for investigation and practical application where folding tessellated arrays of acoustic structures empowers novel power for morphing an aural environment and modulating acoustic energy transmission.

Acknowledgments

The authors thank Dr Kazuko Fuchi of the University of Dayton Research Institute and Drs Phil Buskohl, Greg Reich, and James Joo of the Air Force Research Laboratory for many helpful conversations. The authors acknowledge valuable discussions with Curt Graber of Wattre Corp., F Joseph Pompei of Holosonics, and Miha Ciglar of Ultrasonic Audio Technologies that have clarified and enhanced the motivations of this research. The authors are indebted to an anonymous reviewer for many helpful suggestions. RLH acknowledges start-up funds from the Department of Mechanical and Aerospace Engineering at The Ohio State University.

References

- [1] Postema M 2011 *Fundamentals of Medical Ultrasonics* (New York: Spon Press)
- [2] Fink M, Montaldo G and Tanter M 2003 Time-reversal acoustics in biomedical engineering *Annu. Rev. Biomed. Eng.* **5** 465–97
- [3] Harker B M, Gee K L, Neilsen T B, Wall A T and James M M 2014 Phased-array measurements of full-scale military jet noise *Proc. 20th AIAA/CEAS Aeroacoustics Conf. (Atlanta, GA)* AIAA pp 2014–3069

- [4] Simons D G, Snellen M, van Midden B, Arntzen M and Bergmans D H T 2015 Assessment of noise level variations of aircraft flyovers using acoustic arrays *J. Aircr.* **52** 1625–33
- [5] Panda J, Mosher R N and Porter B J 2014 Noise source identification during rocket engine test firings and a rocket launch *J. Spacecr. Rockets* **51** 1761–72
- [6] Eisenmenger W 2001 The mechanisms of stone fragmentation in ESWL *Ultrasound Med. Biol.* **27** 683–93
- [7] Coussios C C, Farny C H, Ter Haar G and Roy R A 2007 Role of acoustic cavitation in the delivery and monitoring of cancer treatment by high-intensity focused ultrasound (HIFU) *Int. J. Hyperth.* **23** 105–20
- [8] Naguib M and Wiley R H 2001 Estimating the distance to a source of sound: mechanisms and adaptations for long-range communication *Animal Behav.* **62** 825–37
- [9] Wilcox P D 2003 Omni-directional guided wave transducer arrays for the rapid inspection of large areas of plate structures *IEEE Trans. Ultrason. Ferroelectr. Freq. Control* **50** 699–709
- [10] Choi J W and Kim Y H 2012 Integral approach for reproduction of virtual sound source surrounded by loudspeaker array *IEEE Trans. Audio, Speech Lang. Process.* **20** 1976–89
- [11] Shin M, Fazi F M, Nelson P A and Hirono F C 2014 Controlled sound field with a dual layer loudspeaker array *J. Sound Vib.* **333** 3794–817
- [12] Elliott S J, Cheer J, Choi J W and Kim Y 2012 Robustness and regularization of personal audio systems *IEEE Trans. Audio, Speech Lang. Process.* **20** 2123–33
- [13] Blackstock D T 2000 *Fundamentals of Physical Acoustics*. (New York: Wiley)
- [14] Steinberg B D 1976 *Principles of Aperture and Array System Design: Including Random and Adaptive Arrays* (New York: Wiley)
- [15] Benesty J, Chen J and Huang Y 2008 *Microphone Array Signal Processing*. (Berlin: Springer)
- [16] Jensen J A *et al* 2013 SARUS: a synthetic aperture real-time ultrasound system *IEEE Trans. Ultrason. Ferroelectr. Freq. Control* **60** 1838–52
- [17] Abdeen A and Ray L 2013 Design and performance of a real-time acoustic beamforming system *Proc. 2013 IEEE SENSORS Conf. (Baltimore, MD)* p 4
- [18] Product Sheet: LRAD 100X. San Diego, CA: LRAD Corporation; 2015
- [19] Array Ring 48-75, AC pro. Berlin: Acoustic Camera; 2012
- [20] Graber C 2016 Unpublished discussions with President of the Wattle Corporation (28 April 2016)
- [21] Gan W S, Yang J and Kamakura T 2012 A review of parametric acoustic array in air *Appl. Acoust.* **73** 1211–9
- [22] Joseph Pompei F 2016 Unpublished discussions with Founder of Holosonics (28 April 2016)
- [23] Pompei F J 2015 Parametric acoustic array *US Patent* 8,953,821
- [24] Ciglar M 2016 Unpublished discussions with CEO of Ultrasonic, audio technologies, Ltd (2 May 2016)
- [25] Ciglar M 2013 Portable directional speaker *European Patent* SI24375
- [26] Liu Y, Genzer J and Dickey M D 2016 2D or not 2D: shape-programming polymer sheets *Prog. Polym. Sci.* **52** 79–106
- [27] Tolley M T, Felton S M, Miyashita S, Aukes D, Rus D and Wood R J 2014 Self-folding origami: shape memory composites activated by uniform heating *Smart Mater. Struct.* **23** 094006
- [28] Schenk M and Guest S D 2013 Geometry of Miura-folded metamaterials *Proc. Natl Acad. Sci.* **110** 3276–81
- [29] Silverberg J L *et al* 2014 Using origami design principles to fold reprogrammable mechanical metamaterials *Science* **345** 647–50
- [30] Lebéé A 2015 From folds to structures, a review *Int. J. Space Struct.* **30** 55–74
- [31] Peraza-Hernandez E A, Hartl D J, Malak R J Jr and Lagoudas D C 2014 Origami-inspired active structures: a synthesis and review *Smart Mater. Struct.* **23** 094001
- [32] Waitukaitis S, Menaut R, Chen B G and van Hecke M 2015 Origami multistability: from single vertices to metasheets *Phys. Rev. Lett.* **114** 055503
- [33] Silverberg J L *et al* 2015 Origami structures with a critical transition to bistability arising from hidden degrees of freedom *Nat. Mater.* **14** 389–93
- [34] Miura K 1985 Method of packaging and deployment of large membranes in space *Report No.* The Institute of Space and Astronautical Science
- [35] Zirbel S A *et al* 2013 Accommodating thickness in origami-based deployable arrays *J. Mech. Des.* **135** 111005
- [36] Fuchi K *et al* 2015 Topology optimization for the design of folding liquid crystal elastomer actuators *Soft Matter* **11** 7288–95
- [37] Fuchi K *et al* 2015 Origami actuator design and networking through crease topology optimization *J. Mech. Des.* **137** 091401
- [38] Lee T U and Gattas J M 2016 Geometric design and construction of structurally stabilized accordion shelters *J. Mech. Robot.* **8** 031009
- [39] Marras A E, Zhou L, Su H J and Castro C E 2015 Programmable motion of DNA origami mechanisms *Proc. Natl Acad. Sci.* **112** 713–8
- [40] Graber C E 2012 Omni-directional acoustic radiator with radial waveguides for submersible multi-transducer array *US Patent* 8,223,592
- [41] Graber C E 2012 Acoustic transducer array *US Patent* 8,311,261
- [42] Demaine E D and O'Rourke J 2007 *Geometric Folding Algorithms* (Cambridge: Cambridge University Press)
- [43] Kinsler L E, Frey A R, Coppens A B and Sanders J V 2000 *Fundamentals of Acoustics* (New York: Wiley)
- [44] Liu S, Lu G, Chen Y and Leong Y W 2015 Deformation of the Miura-ori patterned sheet *Int. J. Mech. Sci.* **99** 130–42
- [45] Liu X, Yao S, Georgakopoulos S V, Cook B S and Tentzeris M M 2014 Reconfigurable helical antenna based on an origami structure for wireless communication system *Proc. 2014 IEEE MTT-S Int. Microwave Symp.* pp 1–4
- [46] Bildik S, Dieter S, Fritzsche C, Menzel W and Jakoby R 2015 Reconfigurable folded reflectarray antenna based upon liquid crystal technology *IEEE Trans. Antennas Propag.* **63** 122–32
- [47] Fuchi K, Buskohl P R, Joo J J, Reich G W and Vaia R A 2015 Resonance tuning of RF devices through origami folding *Proc. 20th Int. Conf. on Composite Materials (Copenhagen, Denmark)* pp 1–10
- [48] Bies D A and Hansen C H 2006 *Engineering Noise Control: Theory and Practice* (London: Spon Press)
- [49] Kummer W H 1992 Basic array theory *Proc. IEEE* **80** 127–40
- [50] Felton S, Tolley M, Demaine E, Rus D and Wood R 2014 A method for building self-folding machines *Science* **345** 644–6
- [51] Shian S, Bertoldi K and Clarke D R 2015 Dielectric elastomer based 'grippers' for soft robotics *Adv. Mater.* **27** 6814–9
- [52] Courtney C R P *et al* 2014 Independent trapping and manipulation of microparticles using dexterous acoustic tweezers *Appl. Phys. Lett.* **104** 154103
- [53] Senesi M and Ruzzene M 2011 A frequency selective acoustic transducer for directional Lamb wave sensing *J. Acoust. Soc. Am.* **130** 1899–907
- [54] Fahy F and Gardonio P 1987 *Sound and Structural Vibration: Radiation, Transmission and Response* (Oxford: Academic)
- [55] Atalla N and Sgard F 2015 *Finite Element and Boundary Methods in Structural Acoustics and Vibration* (Boca Raton, FL: CRC Press)

Origami acoustics: using principles of folding structural acoustics for simple and large focusing of sound energy

Ryan L. Harne* and Danielle T. Lynd

Department of Mechanical and Aerospace Engineering, The Ohio State University, Columbus, OH 43210, USA.

**Correspondence to: harne.3@osu.edu*

Supplementary Information

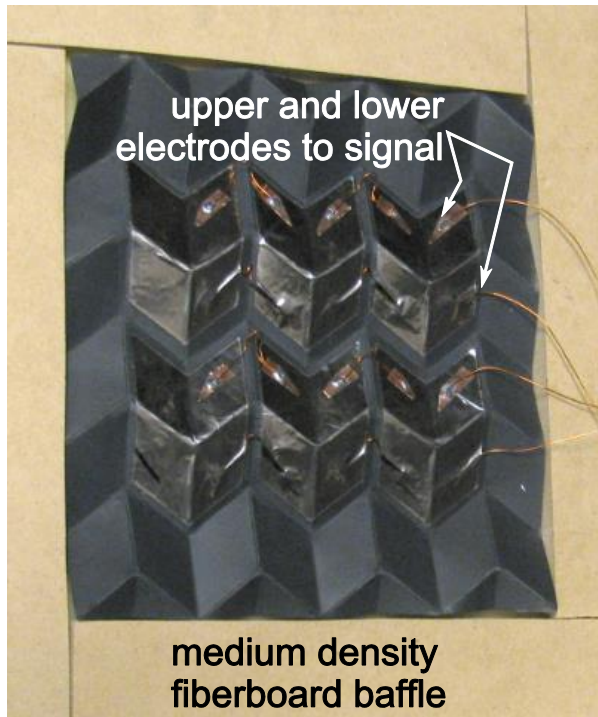
1 Additional discussion and results

The baffling arrangement for the experimental specimen whose measurements are reported in this research is shown in Supplementary Fig. 1.

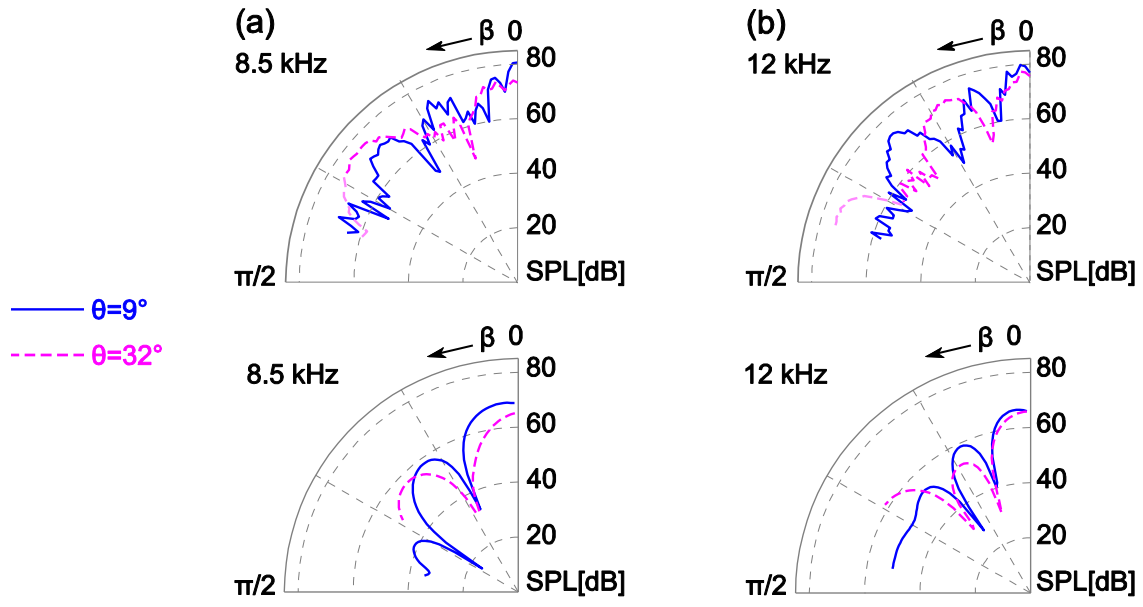
Measurements are taken at 3, 5, 8.5, 9, and 12 kHz. The measurements at 8.5 and 12 kHz, and analytical model prediction comparisons, are presented in Supplementary Fig. 2 with experimental(analytical) data shown in the top(bottom) rows. The evaluation at 8.5 kHz is conducted to help assess the repeatability and consistency of our measurements because the analytical model did not predict significant directivity differences existed between 8.5 and 9 kHz. In agreement with this prediction, our measurements likewise do not reflect significant deviations in the directivity patterns for 8.5 kHz (Supplementary Fig. 2(a), left column) with respect to the measurements at 9 kHz (Fig. 3(c), right column). The evaluation at 12 kHz is carried out because the model predicted numerous pressure nodes away from broadside elevation, which are correspondingly identified in our measurements as seen by the several, sudden reductions in far field SPL for β greater than about $\pi/6$ rad. (15°), see Supplementary Fig. 2(b), right column.

Supplementary Fig. 3 presents the analytical model predictions that correspond to the Audio files 1 to 4 that are measured experimentally. Portions of these audio files are shown in a time series in Fig. 6.

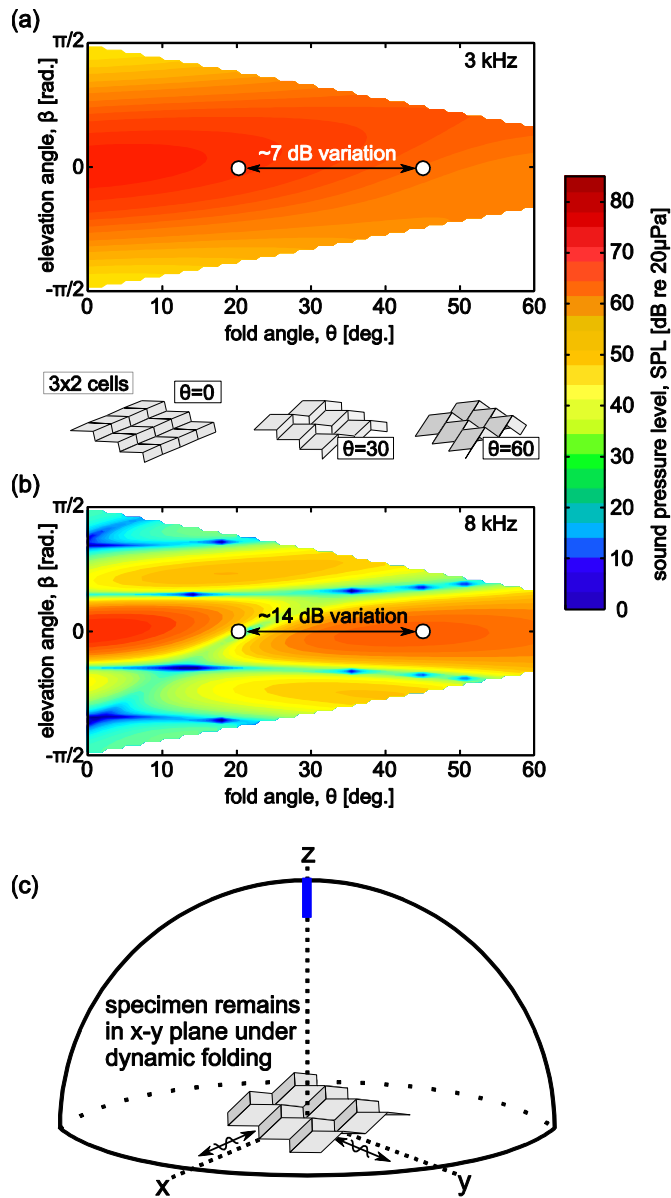
The model parameters utilized to generate the analytical predictions as presented in Figs. 3, 4, 5, and Supplementary Figs. 2 and 3 are as follows: $a=23$ mm, $b=20.9$ mm, $\gamma=50^\circ$, $R=717.55$ mm, and $\omega u_0=200$ m.s⁻² which is a frequency-independent surface acceleration. It is anticipated that the difference between the actual tessellated edge lengths as fabricated in our experimental specimens ($a=33$ mm and $b=30$ mm) and the parameters used to generate model results that agree qualitatively with our measurements ($a=23$ mm, $b=20.9$ mm), is explained the fact that the scaled-down PVDF transduction elements, which perform the vibroacoustic energy conversion, span dimensions closer to $a=23$ mm, $b=20.9$ mm (see Section 2 on PVDF film design and application).



Supplementary Figure 1. Baffled 3x2 cell tessellated array during experimental stages, showing the electrode leads which are connected to the single frequency excitation signals. The two pair of leads are driven in parallel at the final amplification stage.



Supplementary Figure 2. Sound pressure level (SPL, dB ref. 20 μPa) of the acoustic array having 3x2 cells of tessellations as a function of the far field observation point elevation angle β . Measurements (top row) and analytical model predictions (bottom row). Single frequency transducer excitation at (a) 8.5 kHz and (b) 12 kHz.



Supplementary Figure 3. Far field SPL of an acoustic array of 3x2 cells of Miura-ori tessellations as a function of elevation angle β and fold angle θ . Analytical predictions of SPL at (a) 3 kHz and (b) 8 kHz. The circle points denote the values of SPL used to generate the analytical reconstruction parts of Audio files 1 to 4 which precede the experimental measurements. (c) Illustration of the procedure to measure the SPL variation under dynamic folding.

Audio file 1. Full-speed playback. The excitation frequency is at 3 kHz. In the experimental recording portion, the input signal and amplified voltage remain the same throughout the measurements. The first 5 seconds of the audio file are analytical model reconstructions of the predicted sound pressure level variation by modulating the 3x2 Miura-ori transducer array from the fold angles approximately θ of 20 to 45° in a sinusoidal manner. The values from which the analytical reconstruction are derived are shown in Supplementary Fig. 3(a). The remainder of the audio file is the corresponding experiments. The experiments are performed in the semi-anechoic chamber by holding the Miura-ori experimental specimen, seen in Fig. 2(a), in hand and folding it back and forth between fold angles of approximately 20 to 45° while the amplified, single-frequency input signal remains constant. While dynamically folding the specimen in this way, the configuration is held such that it remains in the $x - y$ plane and continues to point the broadside position at the microphone (PCB Piezotronics 130E20) which is in the far field, as illustrated in Supplementary Fig. 3(c).

Audio file 2. Same as Audio file 1 but half-speed playback.

Audio file 3. Same audio material presentation method as for Audio file 1 but the excitation frequency is at 8 kHz. The corresponding analytical predictions to the 8 kHz excitation frequency are presented in Supplementary Fig. 3(b).

Audio file 4. Same as Audio file 3 but half-speed playback.